Materials Advances

ROYAL SOCIETY OF CHEMISTRY

PAPER

View Article Online
View Journal | View Issue

Cite this: *Mater. Adv.*, 2025, 6, 7395

Electrochemical detection of glucose and nitrophenol using a novel CuMn-LDHs/r-GO nanocomposite

Sumbal Tahir,[ab] Farhat Saira,*[a] Hira Noor[b] and Humaira Razzaq*[b]

Layered double hydroxides (LDHs) are gaining interest in multifunctional materials due to their uniform metal ion distribution and ease of anion exchange, contributing to advancements in clinical, environmental, and food chemistry. In this study, Cu–Mn layered double hydroxides (CuMn-LDHs) were synthesized using a one-step co-precipitation method. The pristine LDHs cause aggregation and have limited conductivity. Due to these limitations, reduced graphene oxide (r-GO) was incorporated into CuMn-LDHs and CuMn-LDHs/r-GO nanocomposites were synthesized. Reduced graphene oxide having high surface area caused increased dispersion of CuMn-LDHs and prevented agglomeration. The CuMn LDHs and CuMn-LDHs/r-GO nanocomposites were characterized by using Fourier transform infrared spectroscopy (FTIR), diffuse reflectance spectroscopy (DRS), UV-Vis spectroscopy, scanning electron microscopy (SEM), and X-ray diffraction (XRD). The CuMn-LDH modified gold electrode (CuMn-LDHs/AuE) exhibited electrocatalytic behavior achieving a low detection limit (LOD) of 0.006 μM, with a wide linear range of 50 μM to 6 mM and a sensitivity of 52.28 μA mM^{-1} cm^{-2}. The composite material showed superior performance as a CuMn-LDH/r-GO modified gold electrode (CuMn-LDHs/r-GO/AuE) exhibited good electrocatalytic glucose oxidation, achieving a low detection limit (LOD) of 0.96 nM, with a linear range of 50 μM to 8.6 mM along with a sensitivity of 339.7 μA mM^{-1} cm^{-2} for glucose and a very high sensitivity of 9668 μA mM^{-1} cm^{-2} for nitrophenol (NP). The future potential of these electrode materials to develop sensors is demonstrated by their outstanding quantitative performance, cost effectiveness, and ease of use in a one-step synthesis process.

Received 15th May 2025,
Accepted 20th August 2025

DOI: 10.1039/d5ma00492f

rsc.li/materials-advances

1. Introduction

The simultaneous/dual detection of biologically and environmentally significant analytes has gained considerable attention in recent years, driven by the urgent need for reliable, rapid, and cost-effective sensing technologies.[1–5] Glucose monitoring is critical for managing diabetes and other metabolic disorders. Diabetes is becoming a prevalent, chronic, worldwide health burden condition that can be lethal. In comparison to other illnesses, it can lead to problems including blindness, stroke, cardiovascular disease, and renal failure. Being a chronic condition, diabetes may be made easier to manage by routinely checking blood glucose levels.[1] On the other hand, the organic aromatic molecule 4-nitrophenol (4-NP), which is frequently present in aquatic habitats, is a dangerous chemical contaminant and an essential component of dyes, pesticides, medications, and leather products. Since prolonged exposure to 4-NP can harm the neurological system and impede the flow of oxygen to the blood, the World Health Organization (WHO) have classified it as an extremely hazardous chemical, with an acceptable limit in drinking water set at 1 μg L^{-1}. The specific effects of 4-NP include inflammation, ocular discomfort, and liver damage. It is imperative to identify and remove 4-NP from wastewater and agricultural runoff, or convert it into a less hazardous form.[2] The dual monitoring of such chemically distinct analytes demands sensor materials with high sensitivity, selectivity, and electrochemical versatility.

Numerous techniques, including spectrophotometry, capillary electrophoresis, electrochemical approaches, chromatography, fluorescence, and Raman scattering, have been developed in recent years to detect glucose and nitrophenol. Among them, the electrochemical method has drawn the most attention due to its high sensitivity, selectivity and convenience.[3] Enzyme-based and non-enzymatic glucose sensors are the two available sensors. Enzyme-based sensors employ glucose oxidase or glucose dehydrogenase to catalyze electrochemical processes;

[a] *Nanoscience and Technology Division, National Centre for Physics, Shahdra Valley Road, Islamabad 44000, Pakistan. E-mail: fsghaus@gmail.com, farhat.saira@ncp.edu.pk*
[b] *Department of Chemistry, University of Wah, Quaid Avenue, Wah 47040, Pakistan. E-mail: humaira.razzaq@uow.edu.pk*

however, their application is limited by several drawbacks. For instance, unstable glucose sensors might result from the enzymes being readily denatured during the immobilization process. Additionally, the temperature of the surrounding environment and the chemicals utilized in the detecting system might affect the sensing effectiveness. Therefore, a lot of effort has gone into creating non-enzymatic glucose sensors, particularly those that use direct electrocatalysis of glucose on electrochemically active materials, which have the benefits of low detection limits and high sensitivity.

Third-generation biosensors that use nanomaterials as a non-enzymatic sensing element are being thoroughly studied in this respect. The sensitivity, quick detection, affordability, and long-term stability of these non-enzymatic sensors, which are based on a variety of materials, have made them popular. Here, two-dimensional (2D) materials play a critical role due to improved electrical, optical, chemical, and physical characteristics, making them a distinct class of nanomaterials. Their hallmark qualities are phase, crystallinity, degree of exfoliation, stability, and size.[4] As possible electrode materials for the production of extremely sensitive sensors, black phosphorus (BP), graphene and its oxides, transition metal chalcogenides (TMDCs), metal oxides, and layered double hydroxides (LDHs) have recently been exploited.[5–18] A potential class of non-enzymatic electro-chemical sensor nanomaterials with distinctive two-dimensional molecular hierarchies and superior electrical characteristics are transition metal layered double hydroxides (TM LDHs).[7] Hydrotalcite (HT)-like materials, sometimes referred to as layered double hydroxides (LDHs), are a class of two-dimensional (2D) anionic clay minerals having layered characteristics. With a generic formula of $[M_{1-x}^{2+}M_x^{3+}(OH)_2(A^{n+})_{x/n}]\cdot yH_2O$, many compositions and architectures of LDHs can be created by altering the interlayer anion or modifying the metal components. M^{2+} and M^{3+} represent the layers of divalent and trivalent metallic ions, respectively.[8,9] Membranes, supercapacitors, drug delivery, electrocatalysis, and electrochemical sensors are just a few of the numerous uses for LDHs. Extensive research has verified that these materials are unique due to their large porosities, suitable interlayer gaps, good ion exchange capacities, and highly adjustable internal and two-dimensional architectures.[10]

Layered double hydroxides (LDHs), based on transition metals such as copper (Cu) and manganese (Mn), have been widely explored for electrochemical applications due to their unique layered structured, redox activity, and ion-exchange capabilities. Cu–Mn is well recognized as a significant catalyst due to its availability, low cost, and variety of valence states.[11] Cu–Mn LDHs offer multiple oxidation states that facilitate electron transport processes, making them suitable for redox-based detection mechanisms. Despite their attractive features, the poor conductivity of LDHs remains a limitation for direct application in electrochemical sensing.

To overcome this drawback, conductive carbon-based materials such as graphene oxide (r-GO) are integrated with LDHs. r-GO provides a high surface area, excellent electrical conductivity, and chemical stability, enabling efficient charge transfer and improving the overall electrochemical performance of the composite. The combination of CuMn-LDHs with r-GO can thus create a synergistic nanocomposite with improved sensitivity and selectivity for dual analyte detection. Considering these advantages, the present study is focused on the synthesis and characterization of a novel CuMn-LDHs/r-GO nanocomposite and its application in electrochemical sensing of glucose and nitrophenol. The motivation behind this work lies in developing a multifunctional, cost-effective sensing platform capable of addressing both biomedical and environmental challenges. This study aims to demonstrate the potential of CuMn-LDHs/r-GO as an efficient dual-functional material for sensing applications.[12]

2. Methodology

2.1. Materials and instrumentation

Copper sulphate pentahydrate ($CuSO_4\cdot5H_2O$, Merck, ≥99.9%), manganese carbonate tetrahydrate ($MnCO_3\cdot4H_2O$, Sigma-Aldrich, ≥99.9%), sodium nitrate ($NaNO_3$, Sigma-Aldrich, ≥99.0%), sodium hydroxide (NaOH, Sigma-Aldrich, ≥99.5%), ethanol (C_2H_5OH, Sigma-Aldrich, ≥97.0%), polyvinyl alcohol ($CH_2{=}CHOH$, Sigma-Aldrich, ≥99.5), graphene oxide ($C_XO_YH_Z$, Sigma-Aldrich, ≥99.5), hydrazine (N_2H_4, Sigma-Aldrich, ≥99.5), 4-nitrophenol ($C_6H_5NO_3$, Sigma-Aldrich, ≥99.5), and 0.1 M PBS solution were purchased and used without further purification. De-ionized (DI) water was utilized to prepare all the solutions.

A Joel JDX-11 model device was used to produce XRD spectra using a Cu-Kα (λ = 1.5418 Å) source running at 45 kV. An EDX unit-equipped field-emission scanning electron microscope (ZEISS Sigma 500VP) was used to acquire the SEM morphological pictures and elemental analysis. A PerkinElmer Lambda 900 UV-visible spectrophotometer was used to record the UV-visible spectra of the colloidal dispersions of the produced nanomaterials in aqueous solutions. The electrochemical tests were performed at room temperature using a Gamry 1000 potentiostat.

2.2. Synthesis of pristine CuMn-LDHs

To prepare copper–manganese layered double hydroxides (CuMn-LDHs), stoichiometric amounts of copper and manganese salts (specifically carbonates and sulphates) were dissolved in deionized water to form a clear, homogeneous solution. The molar ratio of Cu^{2+} to Mn^{2+} was precisely controlled in the range of 1 : 1 to 1 : 2, depending on the desired composition of the final material. Aqueous NaOH solution was then added dropwise under continuous stirring to initiate co-precipitation, maintaining the pH at approximately 11.7. This step was crucial to facilitate the formation of a layered hydroxide structure through the controlled nucleation and growth of metal hydroxide sheets. The resulting suspension was aged at room temperature for 24 hours to promote crystallization and enhance the stacking of the hydroxide layers, a critical factor in achieving a well-defined LDH structure. After aging, the precipitates were separated by vacuum filtration and thoroughly washed with deionized water followed by a 20%

ethanol solution to remove residual soluble ions and by-products. The purified solid was then dried at 60–100 °C for 24 hours in an oven. The final product was obtained as a blackish powder.[13]

2.3. Synthesis of CuMn-LDHs/r-GO

CuMn/r-GO was synthesized using a one-pot co-precipitation technique. Graphene oxide (GO) was ultrasonically dispersed into a flask that contained 150 mL of NaOH and Na_2CO_3 solution. Next, 150 mL of distilled water with Cu $(SO_4)_2$ and Mn $(CO_3)_2$ salts was vigorously stirred. Then a solution of sodium hydroxide was added to keep the pH of the resulting solution at 10.5. Prior to being stirred at reflux temperature at 95 °C, the resultant mixture undergoes heating to 60 °C. After that, hydrazine was gradually added to the formed slurry. In the synthesis of copper–manganese layered double hydroxides (CuMn-LDHs) combined with reduced graphene oxide (rGO), here hydrazine hydrate ($N_2H_4{\cdot}H_2O$) is used as a reducing agent to convert graphene oxide (GO) into rGO by addition of hydrogen, during the composite formation process. It removes oxygen-containing functional groups (*e.g.*, hydroxyl, epoxy, carboxyl) from the GO sheets, thus restoring the sp^2 carbon network and converting GO into rGO. Then the resultant slurry was centrifuged at 12 000 rpm, washed with deionized water and 20% ethanol solution, and dried in an oven for 24 hours at 95 °C following six hours of refluxing.[14]

2.4. Electrochemical measurements

A three electrode set-up was used for the electrochemical studies, *i.e.*, a modified gold electrode (AuE) as a working electrode with a surface area of 0.098 cm^2, platinum as a counter electrode, and Ag/AgCl as a reference electrode. An optimized potential window of −0.4 to 1.2 V was used to record cyclic voltammograms. Because the layered double hydroxides need a high alkaline pH (more than 10) for catalytic oxidation, the studies were conducted in 0.05 M NaOH. To optimize the concentration of the sensing material for the working electrode, many test runs were conducted. As previously indicated, 2 mg of nanostructure suspension in 2 mL of DI water was the optimal concentration that produced the best current. When the concentration is increased to 5 mg, the sensing material starts to leak out of the electrode. Using a Gamry interface 3000, EIS investigations were conducted in the frequency range of 0–18 K.

2.4.1. Modification of the working electrode for glucose sensing. Before each measurement, alumina powder (0.05 μm) was used to polish the working electrode, which was then washed with distilled water for five minutes in an ultrasonic bath. In order to modify the gold electrode, 5 μL of a suspension of nanostructures (2 mg/2 mL) in DI water was deposited using the drop casting technique. Following the modification, the electrode was dried for 12 hours at 60 °C in an oven

3. Results and discussion

3.1. XRD analysis

XRD was employed to confirm the crystalline structure and average particle size for CuMn-LDHs and CuMn-LDHs/r GO.

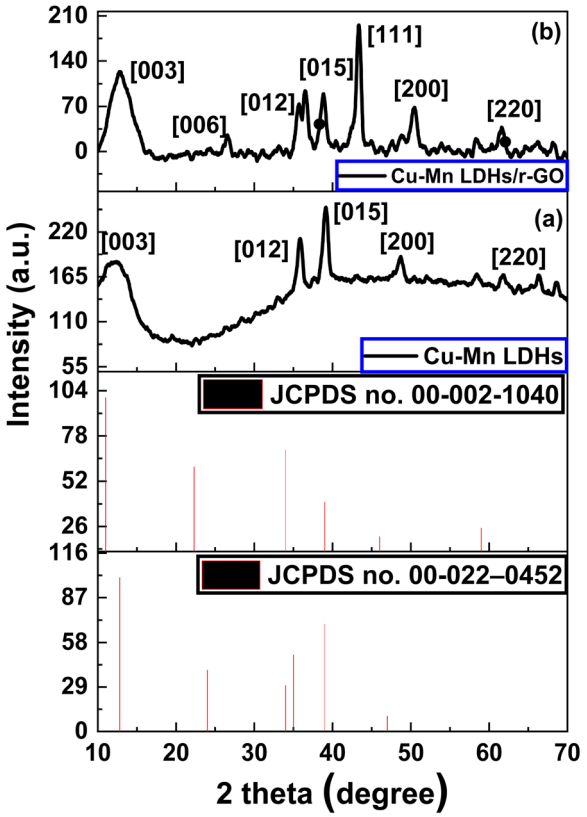

Fig. 1 XRD of Cu–Mn LDHs (a) and Cu–Mn LDHs/r-GO (b).

In Fig. 1, the spectra are shown. To find out the phase composition of respective samples, a variety of XRD diffraction patterns were employed. The large peak at 12° in the XRD pattern of CuMn-LDHs/r-GO is attributed to the (003) crystal planes. Graphene oxide's amorphous nature may be understood in relation to its graphite-like structure, which is made up of stacked graphene sheets in a few layers. On the other hand, the diffraction peaks that appeared at 12.70°, 35.9°, 39.1°, 48.60°, and 60.20° for the pure CuMn-LDHs are attributed to the (003), (012), (015), (006), and (220) crystal planes. The development of LDHs is confirmed by the (003), (012), and (015) reflections, which match the lattice planes of hydrotalcite-like layered double hydroxide (LDH) phases. Since their structures are similar and their diffraction peaks are near to one another, all of the additional Cu–Mn diffraction peaks are consistent with the hexagonal phases of $Cu(OH)_2$ and $Mn(OH)_2$.[15,16] The crystallite size is obtained from the well-known Scherrer's equation (eqn (1)),[17]

$$D = k\lambda/\beta\cos\theta \quad (1)$$

where k represents the shape factor with a value of 0.9, λ represents the wavelength of the X-ray source with a value of 1.5406 Å, and β is the full width half maximum (FWHM). The average crystallite size for the Cu–Mn LDHs was 4 nm and the Cu–Mn LDHs/r-GO was 3 nm. The size of the crystals undergoes reduction on doping with r-GO, which leads to a large surface area. These results are consistent with the DRS results presented in Section 3.4.[18,19]

3.2. FTIR analysis

The FTIR spectra of the CuMn-LDHs and CuMn-LDHs/r-GO are displayed in Fig. 2. The CuMn-LDHs spectra exhibit a broad peak of –OH stretching vibrations from the H bonded –OH group at 3300 cm^{-1}, while the interlayer water molecules exhibit bending vibrations at 1632 cm^{-1}. The signal at 1373 cm^{-1} could reflect CO_3^{2-} bending. Every peak below 900 cm^{-1} displayed crystallographic bending and stretching vibrations caused by metal–oxygen bonding.[20] The existence of –C=C from the sp^2 hybridized carbon structure of r-GO is shown by an extra peak at 1520 cm^{-1} in the case of CuMn-LDHs/r-GO.[21] In the case of CuMn-LDHs/r-GO, the OH group exhibits a peak at a higher wavenumber due to the OH stretching vibrations at 3700 cm^{-1}. A 3700 cm^{-1} peak corresponds to free OH, not hydrogen-bonded OH. The interactions between the LDHs and r-GO cause a small shift in some bands which may be due to drying, reduction, or structural changes, which lead to the disruption of the H-bond network, freeing OH groups and shifting the IR peak. The –C=O peak at 1700 cm^{-1} is caused by the remaining oxygenated functional groups on r-GO. FTIR spectra of CuMn-LDHs show M–O and hydroxyl group vibrations, validating the layered structure. These FTIR analytical results can show the presence of each functional group of LDHs, which is evidence of the successful synthesis of LDHs without other impurity phases.[22,23]

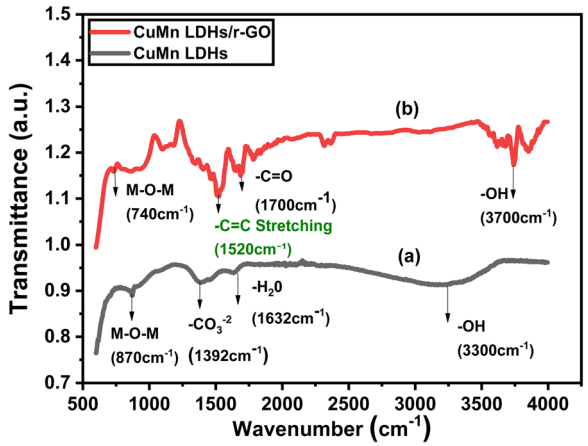

Fig. 2 FTIR spectrum of Cu–Mn LDHs (a) and Cu–Mn LDHs/r-GO (b).

3.3. FESEM and EDX analysis

The surface morphologies of the pristine CuMn-LDH and CuMn-LDH/rGO composites were analyzed through field emission scanning electron microscopy (FESEM). As depicted in Fig. 3a, the pristine CuMn-LDH reveals a distinct, sheet-like layered morphology composed of well-defined nanosheets, although some degree of nanosheet aggregation is evident. Similar features are observed in the CuMn-LDH/r-GO composite (Fig. 3c). To mitigate such agglomeration, it is crucial to develop nanostructures that enable robust and flexible architectures *via* self-assembly mechanisms. The CuMn-LDH/r-GO hybrid composite (Fig. 3c) demonstrates a denser and more compact morphology with a cloud-like appearance, suggesting that the LDH nanosheets are effectively embedded within the reduced graphene oxide (r-GO) matrix. This configuration may

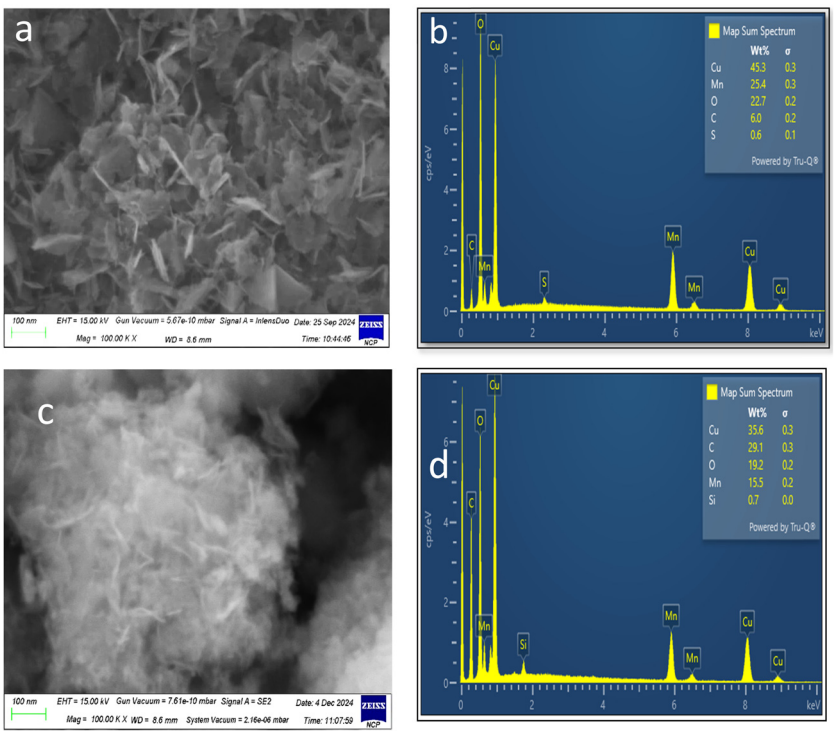

Fig. 3 Surface morphological studies of the synthesized materials using electron microscopy. (a) SEM micrograph of CuMn-LDH, (b) EDX image of CuMn-LDH; (c) SEM micrograph of CuMn-LDH/r-GO and (d) EDX image of CuMn-LDH/r-GO.

reduce the direct exposure of active sites; however, it significantly enhances structural stability and electrical conductivity, which are advantageous for long-term and real-time sensor applications.

FESEM images further confirm the radial orientation of thin LDH lamellae distributed across the r-GO scaffolds. This hierarchical structure, characterized by a large surface area, effectively promotes electrolyte diffusion and enhances the availability of electrochemically active sites. The successful incorporation of r-GO within the CuMn-LDH/r-GO composite is substantiated by energy-dispersive X-ray (EDX) spectroscopy and elemental mapping. As shown in Fig. 3b, in pristine CuMn-LDHs, copper (Cu) and manganese (Mn) are present in relatively high amounts, 45.3% and 25.4%, respectively, indicating a metal-rich layered structure, while oxygen (O) accounts for 22.7%, and carbon (C) remains minimal at 6.0%, consistent with the inorganic nature of the pristine LDHs. But in the case of a composite as shown in Fig. 3d, the CuMn-LDHs/r-GO shows a prominent decrease in both Cu (35.6%) and Mn (15.5%) content, along with a significant increase in carbon content to 29.1%, confirming the successful integration of carbonaceous r-GO sheets within the LDH matrix. The oxygen content remains relatively stable, though slightly reduced to 19.2%.[23,24]

3.4. Diffuse reflectance spectroscopy

The electrical band gap refers to the lowest energy which is required to generate an electron–hole pair in a material (semiconductor). Eqn (2) was used to calculate the bandgap of the synthesized materials. The graph is plotted between $[F(R)\cdot h\nu]^n$ on the y-axis and photon energy ($h\nu$) on the x-axis. The bandgap is evaluated from the intercept of the extrapolated linear part of the graph. On the other hand, the exciton potential that induces vertical interband shifts is the optical band gap. Information on wavelength and reflectance percentage was received. We used a Tauc plot to compute the material's band gap based on this data.

$$(h\nu - E_g)^n = \alpha h\nu \quad (2)$$

where α is the coefficient for absorbance and E_g is the allowed direct bandgap of the semiconductor nanomaterial, $h\nu$ is the energy of a photon, h is Plank's constant, n is the frequency, and the photon energy is $h\nu = 1240/\lambda$.

Fig. 4 displays the Tauc plot of the CuMn-LDHs and CuMn-LDHs/r-GO. Because of the increased electrical conductivity of composites, the bandgap difference between the pure CuMn-LDHs (1.7 eV) and r-GO/CuMn-LDHs nanocomposite (1.6 eV) affects how well they work in glucose sensing applications. CuMn-LDHs feature greater energy transitions, which accelerate electron transport. An enhanced intrinsic conductivity is correlated with a smaller bandgap. This improved the electron transfer efficiency during glucose oxidation.[25–27]

3.5. UV-visible spectroscopy

The UV spectra of CuMn-LDHs and CuMn-LDHs/r-GO are shown in Fig. 5. Both spectra show maximum wavelength at 375 nm. The UV spectrum of the CuMn-LDHs displays bands associated with charge transfer, ligand to metal charge transfer (LMCT) or metal to ligand charge transfer (MLCT). The bands in the UV region between 200 and 400 nm are exhibited by Cu^{2+} due to charge transfer, which are often seen because of electron transfer characteristics. On the other hand, the d^5 configuration of Mn^{2+} shows weak transitions because of its spin-forbidden nature, although it can show up in the UV region, usually between 250 and 380 nm.

The LDH matrix effect affects the precise location and strength of these bands because of the surrounding environment of the metal ions, including the type of intercalated anions and the general symmetry of metal sites.[28,29] Another important aspect is that there is an increase in the intensity of the LDH spectrum after complex formation with r-GO. This enhancement is evident for complex formation and no shift in the main peak positions is observed because of the physical interactions of graphene and the LDHs.

3.6. Thermogravimetric analysis

TGA was used to analyze the thermal stability of CuMn-LDH/rGO. The TGA curve of CuMn-LDHs/r-GO in Fig. 6 revealed that

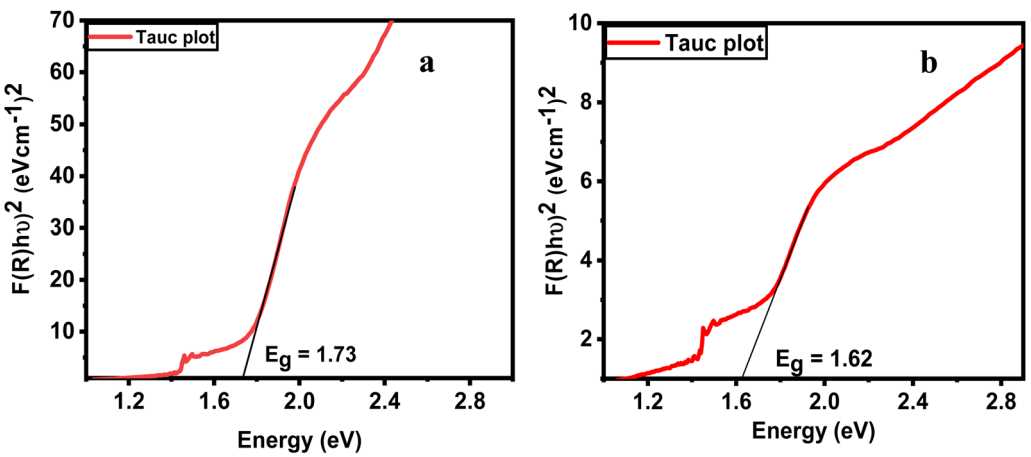

Fig. 4 Tauc plot of Cu–Mn LDHs (a) and Cu–Mn LDHs/r-GO (b).

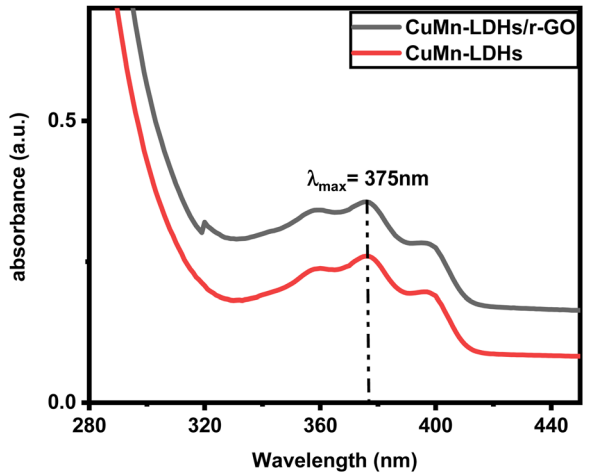

Fig. 5 UV spectra of Cu–Mn LDHs and Cu–Mn LDHs/r-GO.

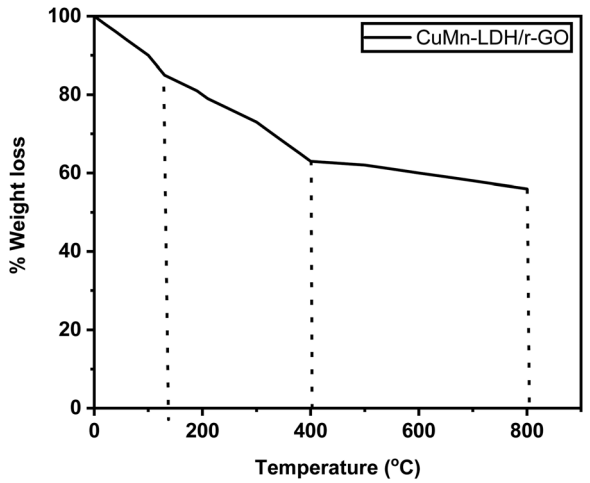

Fig. 6 TGA curve of CuMn-LDHs/r-GO.

a small mass loss occurs due to evaporation of physically adsorbed water molecules present on both CuMn LDHs and r-GO surfaces (140 °C). The subsequent weight losses related to dehydroxylation – the removal of hydroxyl groups as water molecules and oxygen containing functionalities (200–400 °C). The anion present in the LDH structure undergoes decomposition leading to a distinct mass loss step. Above 400 °C, r-GO undergoes oxidative decomposition, leading to minor mass loss. This step is a characteristic of carbonaceous materials and forms mixed metal oxides.[33] The CuMn-LDH/r-GO composite shows a 4–5% weight loss between 400 and 800 °C due to r-GO decomposition, with the total weight loss reaching 40–45% by 800 °C. The gradual loss around 600 °C is linked to the removal of adsorbed water and oxygenated groups, while the presence of r-GO enhances the material's thermal stability.[30]

3.7. Electrochemical sensing analysis

CuMn-LDH and CuMn-LDH/r-GO electroactivity is examined with scan rate. Fig. 7 illustrates how scan rate affects the electrochemical response of the CuMn-LDH and CuMn-LDH/r-GO nanostructures. Voltammograms were recorded in 0.05 M NaOH after the working electrode was fabricated using the optimized concentration. The anodic (I_{pa}) and cathodic (I_{pc}) peak currents both increase linearly as the scan rate increases from 100 to 1000 mV s^{-1}, as seen in Fig. 7, suggesting a diffusion-controlled mechanism.[31] The peak potential also moves toward more positive values as the scan rate increases. The process occurring at the working electrode is quasi-reversible as the anodic to cathodic peak current ratio (I_{pa}/I_{pc}) is less than one.[32]

The CuMn-LDH, and CuMn-LDH/r-GO cyclic voltammetry (CV) curves are shown in Fig. 7a and b, respectively. In an alkaline electrolyte without glucose, a large cathodic peak is observed for CuMn-LDHs between −0.2 and −0.4 V. This is indicative of the reduction of the Cu(II) and Mn(II) centers in the positively charged lamella. The reduction peaks of Cu(II) and Mn(II) ions combine because their redox potentials are near to one another. The reduction reaction of the Cu and Mn core may be identified by the single wide reduction peak observed during the reverse scan at −0.2 to −0.4 V.

The electrode surface response was a diffusion-controlled process, as demonstrated by the graph in Fig. 7c and d that plots peak current (I_p) against the square root of the scan rate ($\upsilon^{1/2}$). The anodic peak current's linear equation was I_{pa} (A), with a regression coefficient (R^2) of 0.9989. The linear plot of a perfectly diffusion-controlled process contains zero intercept; but in this case, double-layer charging in the CuMn-LDH instance upsets this notion.[33] The Randles–Sevcik equation is utilized to find out the diffusion coefficient of a particular analyte (glucose) (eqn (3)).

$$I_p = (2.69 \times 10^5) n^{3/2} A C D^{1/2} v^{1/2} \quad (3)$$

where A is the electrode's active surface area (0.98 cm^2), C is the glucose concentration (1×10^{-3} mol cm^{-3}), D is the diffusion coefficient (cm^2 s^{-1}), v is the scan rate (V s^{-1}), I_p is the peak current, and n is the number of electrons in the half-reaction for the redox pair, here n = 1.[34,35] The diffusion coefficient of the electrons was calculated to be 7.2×10^{-11} cm^2 s^{-1} in the case of CuMn-LDHs, but in the case of the CuMn-LDHs/r-GO composite, the value of diffusion coefficient increases to 3.4×10^{-9} cm^2 s^{-1} using the slope of the linear regression. The increase in the value of D leads to improved mass transport of electroactive species toward the surface of the electrode, resulting in stronger current response and high sensitivity.[36,37]

3.7.1. Estimation of sensitivity, LOD, and linear range of the biosensor. An electrochemical investigation was conducted to detect glucose at a scan rate of 100 mV s^{-1}. No oxidation current was observed in the absence of glucose.[38] However, as the glucose concentration increased from 50 μM to 4.4 mM, the anodic current (oxidation current) responded more strongly. Fig. 8a depicts the oxidation current at various glucose concentrations. Linear regression of this curve is shown in Fig. 8c, and from the slope of this plot the sensitivity was calculated. For CuMn-LDHs, the obtained sensitivity value was 52 μA mM^{-1} cm^{-2}. Using eqn (4),

$$\mathrm{LOD} = 3\sigma/s \quad (4)$$

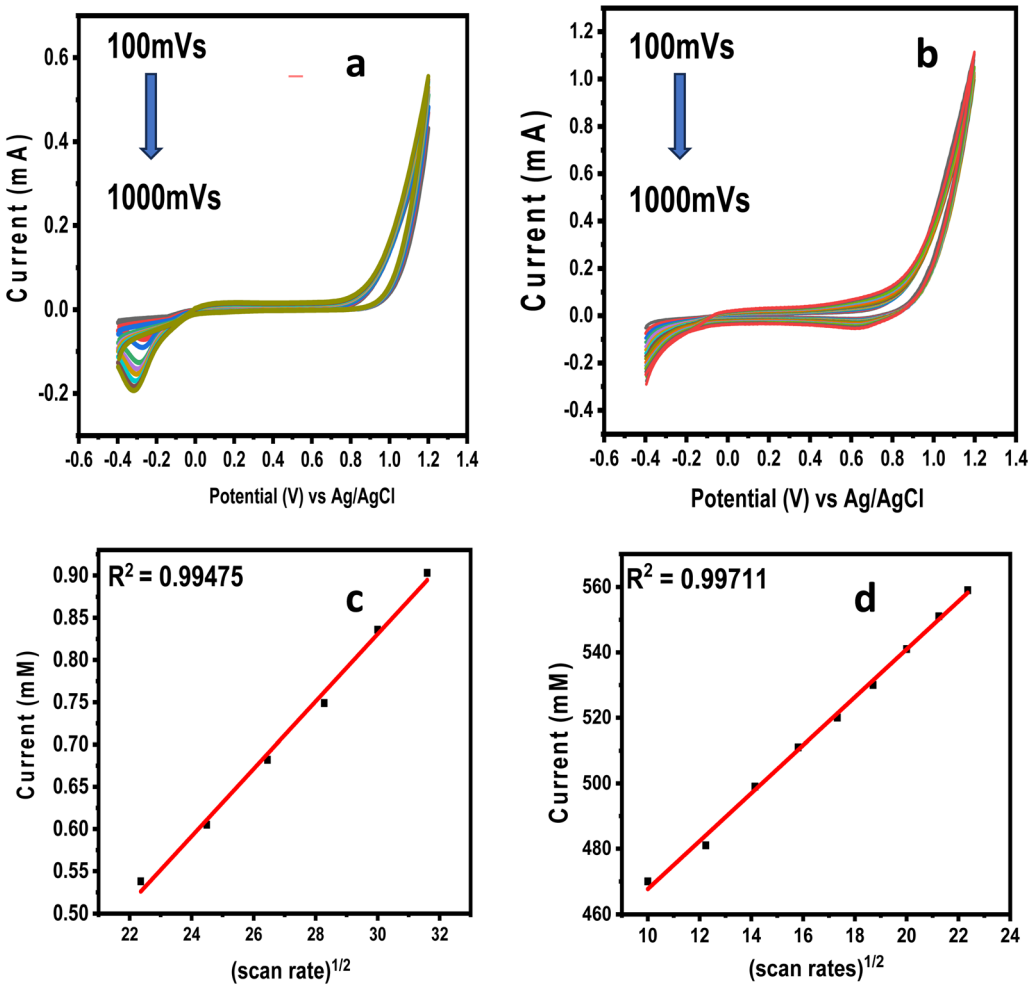

Fig. 7 Cyclic voltammogram of (a) CuMn-LDHs, (b) CuMn-LDHs/r-GO modified AuE recorded in 0.05 M NaOH at varied scan rates (100–1000 mV s^{-1}), (c) and (d) the linear regression curves for (c) CuMn-LDHs and (d) CuMn-LDHs/r-GO modified AuE as a plot between the square root of scan rate and anodic peak current.

the limit of detection was found to be 0.006 μM, where s is the slope value derived from the calibrated plot and σ is the standard deviation derived from blank signals.[39,40] It was evident from the literature, as shown in Table 1, that the LDH nanocomposite provides superior sensitivity even at lower glucose concentrations depicting that the material was more sensitive. Similarly, cyclic voltammetry was used to electrochemically analyze CuMn-LDH/r-GO, for glucose sensing (Fig. 8b).

All the parameters were identical, and current oxidation was simultaneously investigated at various glucose concentrations. Fig. 8b illustrates the behavior of the anodic current at different glucose concentrations. The CuMn-LDH/r-GO nanocomposite's sensitivity from linear regression (Fig. 8d) was found to display the CuMn-LDH/r-GO nanocomposite's sensitivity and limit of detection in relation to other reported nanocomposites.

3.7.2. Mechanism of electro-oxidation at the electrode surface. The synergistic impact produced by combining CuMn LDHs/r-GO is demonstrated by the enhanced sensitivity of CuMn-LDHs/r-GO/AuE. Considering the pure MnO_2 component lacked electrocatalytic activity, it had an effect on the interfacial electron transport pathway. When glucose was introduced, the anodic peak current increased as predicted, and as the amount of glucose increased, the peak intensity also increased. When glucose is added, the anodic peak current increases significantly but the cathodic peak current barely changes. The conversion of glucose to gluconolactone, which is subsequently hydrolyzed into gluconic acid, is electrocatalyzed by the CuMn-LDHs/r-GO electrode. Reduced graphene oxide improves the conductivity and electron transfer kinetics. It acts as a conductive substrate that disperses the CuMn-LDH nanoparticles and increases the surface area for catalytic applications. When glucose is added, it undergoes oxidation at the CuMn-LDHs. The electron was released during the oxidation of glucose through the r-GO network generating a current, which is directly proportional to the amount of glucose. The following reaction can be used to characterize the possible oxidation process of glucose on the LDH surface. With the exception of the greater redox current, the electrochemical behavior of CuMn-LDHs/r-GO is almost the same as that of a pure CuMn-LDH sample, both with and without glucose.[41–43] The mechanism

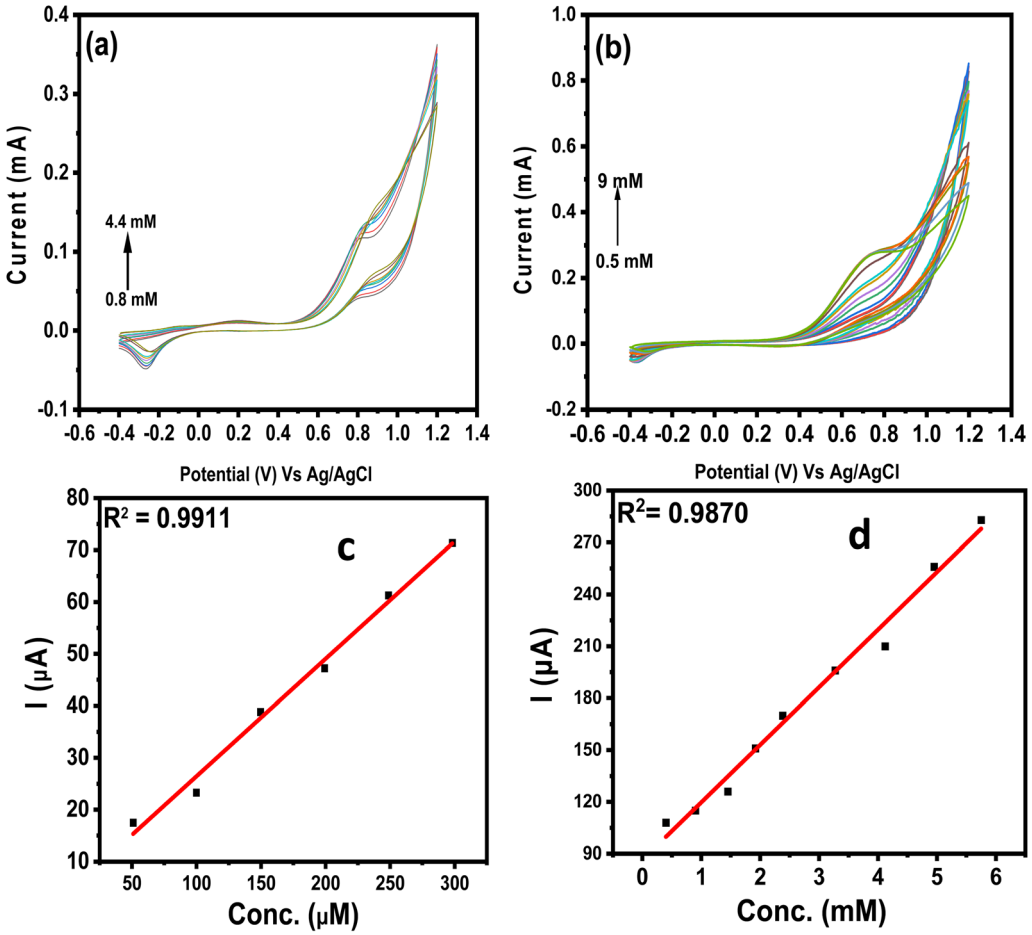

Fig. 8 (a) and (b): CuMn-LDHs (a) and CuMn-LDHs/r-GO (b) responses against different concentrations of glucose; (c) and (d): calibration plot of anodic maximum current *vs.* the concentration of glucose in the case of (c) CuMn-LDHs and (d) CuMn-LDHs/r-GO.

Table 1 Comparative analysis of various types of LDH in terms of catalytic behavior from the literature

S. no	Electrode materials	Linear range (μmol L^{-1}–mmol L^{-1})	Limit of detection (μmol L^{-1})	Sensitivity (μA m M^{-1} cm^{-2})	Ref.
1	Au/LDH-CNTs-G	1–0.35	0.5	189	44
2	NiFe LDH nanosheets	1–5.7	0.2	—	45
3	Graphene QDs/CoNiAl-LDH nanocomposites	10–14.0	6	48.717	46
4	PAN/PAni/graphene	10–1.97	2.10	29.11	47
5	At low conc.	50–0.9	0.141	2.30	
	CuMn LDHs (glucose)				Current work
6	At high conc.	50–6	0.006	52.28	
	CuMn LDHs (glucose)	0.9–5	1196.29	0.0557	Current work
	CuMn LDHs (NP)				
7	CuMn LDHs/r-GO	50–8.6	0.000962	339.7	
	CuMn LDHs/r-GO (NP)	0.9–75	28.53	9668	Current work

of electron transfer by glucose to metallic LDH is as follows (eqn (5)–(8));

$$\text{LDH-Cu(II)} + OH^- \rightarrow \text{LDH}(OH^-)\text{-Cu(III)} + e^- \quad (5)$$

$$\text{LDH-Mn(II)} + OH^- \rightarrow \text{LDH}(OH^-)\text{-Mn(III)} + e^- \quad (6)$$

$$\text{LDH}(OH^-)\text{-Cu(III)} + \text{glucose} \rightarrow \text{LDH}(OH^-)\text{-Cu(II)} + \text{gluconolactone} \quad (7)$$

$$\text{LDH}(OH^-)\text{-Mn(III)} + \text{glucose} \rightarrow \text{LDH}(OH^-)\text{-Mn(II)} + \text{gluconolactone} \quad (8)$$

3.7.3. Electrochemical impedance spectroscopy (EIS) studies. Electrochemical impedance spectroscopy (EIS) was used to examine the characteristics of the electrochemical interface on the modified electrodes. These impedance graphs were simulated

using the constant phase element (CPE), Randles circuit, which contains the Warburg element (W), charge transfer resistance (R_{ct}), and electrolyte resistance (R_s) shown in Fig. 10. The study found that quicker electron transit between the modified electrodes and electrolytes was linked to lower R_{ct} values. The Nyquist plots of the bare AuE, CuMn-LDHs, and CuMn-LDHs/r-GO are displayed in Fig. 9.

The diameter of the observed semicircle in the EIS curves represents the charge transfer resistance (R_{ct}) as a result of the faradaic processes. In this case, CuMn-LDHs/r-GO shows a smaller semicircle meaning that it has the least charge transfer resistance (R_{ct}), which indicates high electrochemical conductivity. The curve crossing on the real axis in the high-frequency zone indicates the internal resistance (R_s) of the electrochemical system.[48] In the case of CuMn-LDHs/r-GO, it has the lowest solution resistance improving ion transport at the electrode–electrolyte interface, which improves significantly the electrochemical performance of the sensor. The CPE values showed that the nanocomposite's porosity and roughness were increased. Fast adsorption onto the electrode surface and enhanced ion transport into the electrolyte are depicted by the vertical line.

We also calculated the electrical conductivity (σ) measurements of the Au bare electrode, CuMn-LDHs, and a CuMn-LDHs/r-GO nanocomposite. Conductivity was evaluated by first measuring the solution resistance (Ru) using electrochemical

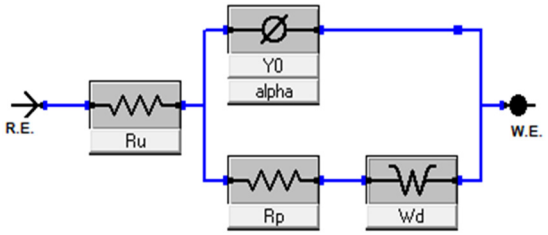

Fig. 10 Circuit diagram of EIS of the modified electrode of CuMn-LDHs and the CuMn-LDHs/r-GO electrode.

impedance spectroscopy and then applying the standard equation (eqn (9)) for conductivity:

$$\sigma = L/(R \times A) \quad (9)$$

where L is the length between electrodes (1 cm), R is the measured resistance (Ru), and A is the cross-sectional area of the electrode (0.98 cm^2).[49] The bare electrode exhibited the highest resistance value of 933 Ω, resulting in a very low conductivity of 1.53×10^{-4} S cm^{-1}, indicating poor charge transport. Upon modification with Cu–Mn LDHs, the resistance dropped significantly to 199 Ω, increasing the conductivity to 7.17×10^{-3} S cm^{-1} given in Table 2, which demonstrates improved electron transfer due to the layered structure of the

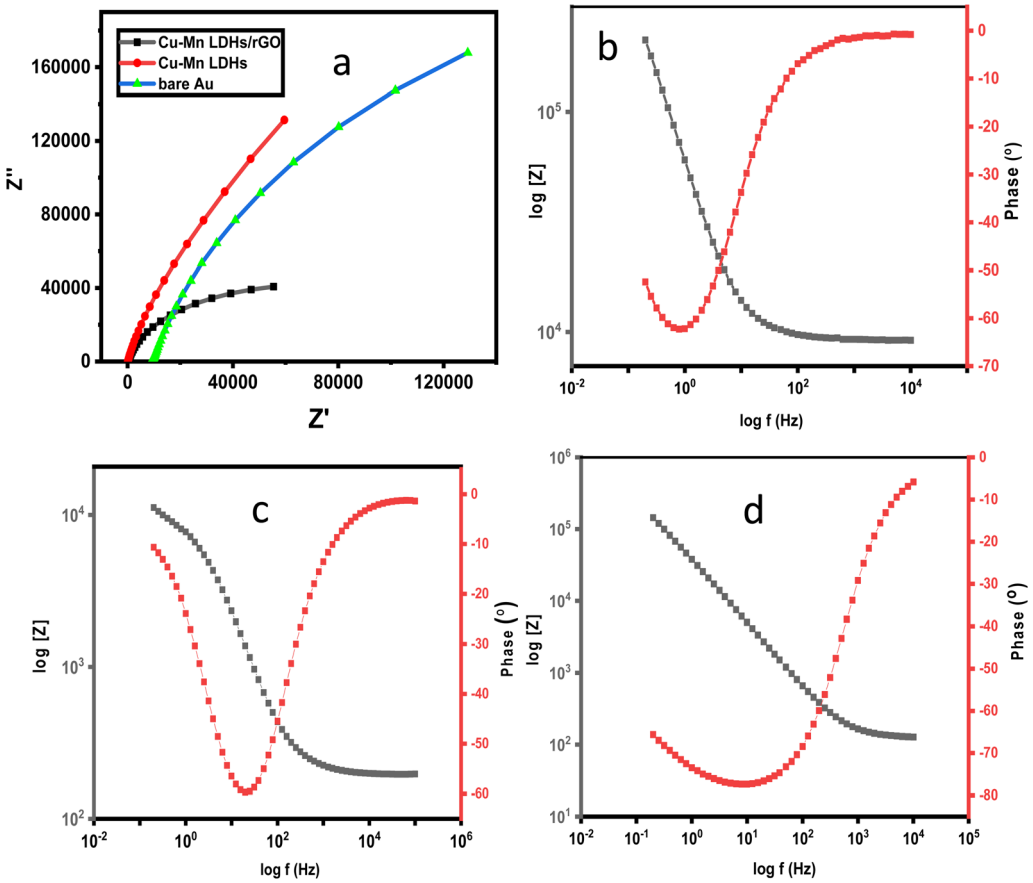

Fig. 9 Nyquist plot of LDH modified AuE in 0.05 M NaOH (a) and Bode plots of bare AuE (b), CuMn-LDHs (c) and CuMn-LDHs/r-GO (d).

Table 2 Comparative analysis of conductivity (σ) measurement of LDH pristine and composite materials

Circuit element	Bare Au	Cu–Mn LDHs	Cu–Mn LDHs/r-GO
Ru (Ω)	933	199	130.7
σ (S cm^{-1})	1.53×10^{-4}	7.17×10^{-3}	0.01

LDHs that facilitate ionic diffusion. Further improvement was observed with the addition of reduced graphene oxide (r-GO) to form the CuMn-LDHs/r-GO composite. This composite showed the lowest resistance value of 130.7 Ω and the highest conductivity of 0.01 S cm^{-1}, highlighting the superior conductive nature of r-GO. The incorporation of r-GO provides an interconnected conductive network, accelerating electron mobility and significantly boosting the electrochemical performance of the material. This increasing trend in conductivity from bare to Cu–Mn LDHs and then to CuMn-LDHs/r-GO confirms the synergistic effect of the LDH matrix and r-GO. It is important to note that the conductivity values of these prepared materials have not been reported previously in the literature, which underlines the novelty and potential of the synthesized nanocomposite for applications requiring efficient charge transport mostly in electrochemical devices.

In the case of the Bode plot, at low frequencies, the system showed capacitive behavior because charges accumulate at the interface, leading to high impedance as the current mainly charges the capacitor. At high frequencies, resistive behavior dominates since there is not enough time for charge storage, allowing current to flow more freely and resulting in lower impedance.[50] As in the case of the Bode plot of CuMn-LDHs displayed in Fig. 9c, the phase shift of -65° indicates that the total impedance at low frequencies is a mixture of resistive and capacitive components rather than being entirely capacitive because phase shift ϕ equal to 90° is for perfect capacitive behavior. The phase shift in the case of CuMn-LDHs/r-GO shown in Fig. 9d is quite small at low frequencies but grows to -80° at high frequencies indicating a dominating rise in capacitive behavior.[51]

3.7.5. Electrochemical behavior of CuMn-LDHs and CuMn-LDHs/r-GO towards 4-NP sensing. The electrochemical performance of the modified electrodes was assessed using cyclic voltammetry (CV) in the presence of 4-nitrophenol (4-NP) in 0.1 M phosphate-buffered saline (PBS) acting as an electrolyte, with scan rates ranging from 100 to 500 mV s^{-1} over a potential window of -1.1 to 0.1 V. The reductive peak currents increased progressively with increasing scan rate, indicating enhanced

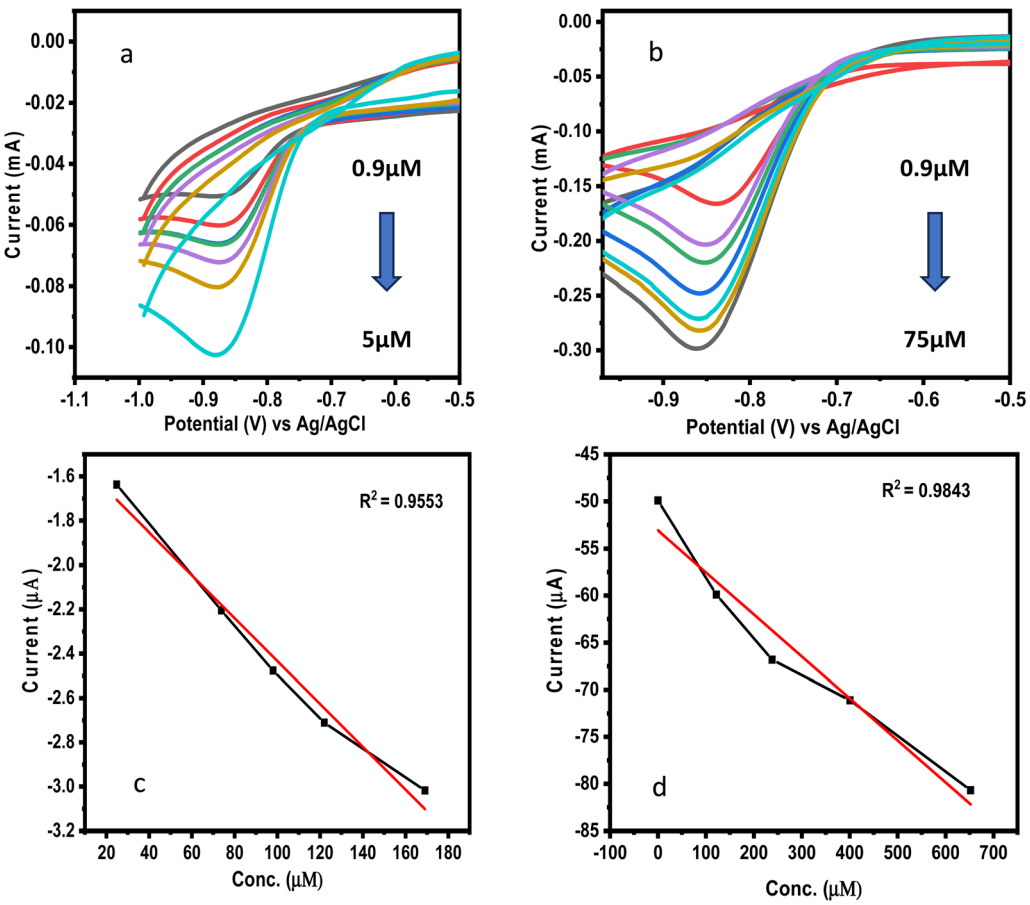

Fig. 11 (a) and (b): CuMn-LDHs (a) and CuMn-LDHs/r-GO (b) responses against different concentrations of nitrophenol (c) and (d): SEM (c) calibration plot of cathodic maximum current *vs.* the concentration of glucose in the case of CuMn-LDHs (d) and CuMn-LDHs/r-GO.

electrochemical activity. Notably, the gold electrode (AuE) modified with CuMn-layered double hydroxides (CuMn-LDHs) exhibited significant improvements in redox peak currents as the 4-NP concentration increased from 0.9 μM to 5 μM as shown in Fig. 11a and b. In contrast, the CuMn-LDHs/r-GO composite showed a broader linear detection range, from 0.9 μM to 75 μM, reflecting improved sensitivity. This enhancement is attributed to the increased adsorption capacity for 4-NP and more efficient electron transfer at the electrode interface. Furthermore, the integration of CuMn-LDHs with reduced graphene oxide (r-GO) substantially boosted the electrode's detection capabilities, achieving a maximum current response of 9668 μA cm^{-2} with a sharp, well-defined redox peak calculated from the regression curves as shown in Fig. 11c and d.

The enhanced electrochemical performance is attributed to the synergistic interaction between the CuMn-LDHs and r-GO, which improves both electrical conductivity and material dispersibility. This synergy results in a more efficient electron transfer process, thereby enhancing the detection of 4-nitrophenol (4-NP). The results indicate that the optimal incorporation of the LDH composite with r-GO significantly boosts electrochemical activity, making the CuMn-LDH/r-GO composite a highly effective platform for 4-NP sensing. A linear relationship (R^2 = 0.995) between current density and the square root of the scan rate shown in Fig. 12a, observed at a potential of −0.8 V, confirms that the electron transfer process is diffusion-controlled. Additionally, the abundant active sites in the CuMn-LDH/r-GO material contribute to facilitating electron transfer, further enhancing the electrochemical detection of 4-NP.

To evaluate electrochemical performance, analyzing the surface properties of the modified electrode is crucial. Electrochemical impedance spectroscopy (EIS), performed in 0.1 M PBS, was used to study the electrode–electrolyte interface, with Nyquist plots as shown in Fig. 12b interpreted using Randles equivalent circuit (including components like Warburg impedance, double-layer capacitance, solution resistance, and charge-transfer resistance, R_{ct}). The Nyquist plots showed that the bare gold electrode (AuE) had the largest semicircular arc, indicating a high R_{ct} and poor charge transfer capability. In contrast, modification with CuMn-LDHs/r-GO significantly reduced the arc diameter, reflecting a lower R_{ct} and improved electron transfer. This reduction suggests enhanced conductivity, efficient ion transport, and better electrochemical responsiveness due to the synergistic properties of the composite material.[13,52,53]

4. Conclusions

Significant developments in electrocatalytic applications are revealed by the synthesis and characterization of CuMn-LDHs and CuMn-LDHs/r-GO. The structural, optical, morphological, and electrochemical characteristics of these synthesized CuMn-LDHs and its composites CuMn-LDHs/r-GO were evaluated using different techniques such as FTIR, DRS, SEM-EDX, XRD, cyclic voltammetry (CV), and electrochemical impedance spectroscopy (EIS). Successful integration of r-GO into the CuMn-LDH backbone was confirmed by FTIR analysis, which showed efficient chemical interaction. DRS showed that the band gap of the composites was less than that of pure CuMn-LDHs, suggesting improved optical properties that could be useful in applications that require charge transfer or light absorption. XRD analysis confirms the successful formation of the CuMn-LDHs/r-GO composite and highlights the structural modifications induced by the r-GO support. SEM-EDX demonstrates that CuMn-LDHs are composed of rough-surfaced, irregular particles that are meant to aggregate, but when r-GO is added, they exhibit a somewhat uniform spherical shape. CuMn-LDHs/r-GO has a greater specific surface area than pure LDHs, suggesting improved electrochemical performance. A successful composite synthesis was shown by the stoichiometric ratios of the precursor in the EDX mapping micrograph. The cyclic voltammetry (CV) of the composites revealed a decrease in

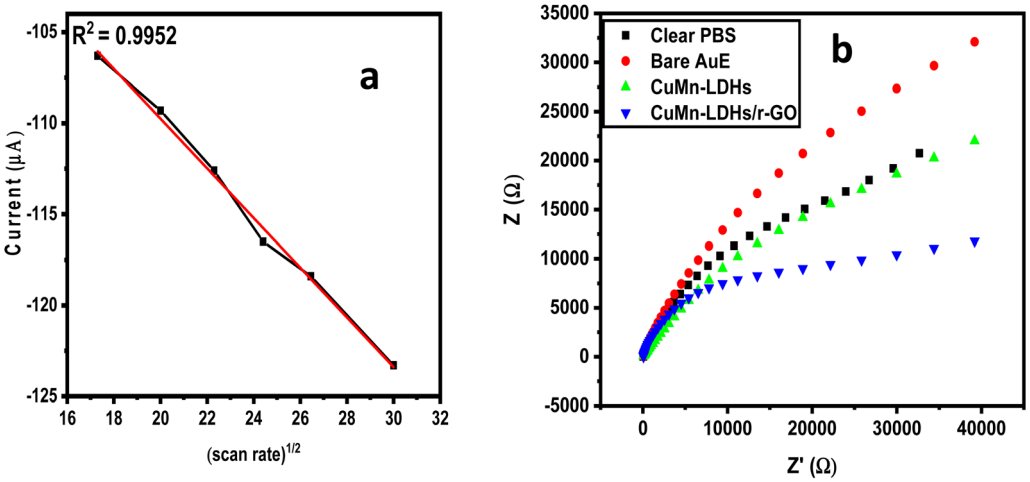

Fig. 12 (a) The linear regression curve for CuMn-LDHs/r-GO as a plot between the square root of scan rate and cathodic peak current and (b) Nyquist plots of 0.1 M PBS (black), bare AuE (red), CuMn-LDHs (green), and CuMn-LDHs/r-GO (blue).

overpotential and an increase in current responsiveness. This behavior points to increased electrochemical performance, better electron transfer, and improved redox activity. The improved charge transfer efficiency is further supported by the decreased band gap of the composites. By showing that the composites had higher conductivity and lower resistance, EIS analysis added further understanding. These findings suggest that the addition of r-GO increases the mobility of the charge carriers, rendering the substance more conductive and appropriate for real-world uses in electronic devices, sensors, and storage. CuMn-LDHs based on transition metals provide exceptional catalytic performance due to their distinct structure, large surface area, and adjustable characteristics. These materials show higher stability, better conductivity, and more active sites when combined with r-GO, all of which are essential for increasing catalytic efficiency. The CuMn-LDH composite shows great promise for the development of inexpensive, portable, and extremely sensitive glucose monitoring devices due to its potential for use in non-enzymatic glucose sensors.

Conflicts of interest

The authors declare no competing financial interest.

Data availability

All data will be made available as required.

Supplementary information is available. See DOI: **https://doi.org/10.1039/d5ma00492f**.

Acknowledgements

The authors acknowledge National Centre for Physics, Islamabad and Wah University for financial and material characterization support.

References

1 J. Zhang, *et al.*, Design and fabrication of NiMn layered double hydroxide/reduced graphene oxide as electrochemical sensor for simultaneous detection of ascorbic acid, dopamine and uric acid, *J. Inorg. Organomet. Polym. Mater.*, 2024, **34**(8), 3660–3674.

2 N. Sivaraman, N. Kumaravel and R. Thangamuthu, Hierarchical NiMnLDH decorated porous carbon nanotubes with N-doped graphitic carbon for electrochemical sensing of 4-nitrophenol, *Microchim. Acta*, 2025, **192**(3), 142.

3 F. Barahuie, M. Z. Hussein, P. Arulselvan, S. Fakurazi and Z. Zainal, Drug delivery system for an anticancer agent, chlorogenate-Zn/Al-layered double hydroxide nanohybrid synthesised using direct co-precipitation and ion exchange methods, *J. Solid State Chem.*, 2014, **217**, 31–41.

4 O. O. Balayeva, T. S. Israfilli and A. A. Azizov, Fullerene (C60)-doped zinc-aluminium layered double hydroxide/polyvinyl alcohol nanocomposites: Synthesis, characterization, and photodegradation of methylene blue from water solution, *J. Chin. Chem. Soc.*, 2024, **71**, 21–34.

5 T. Li, *et al.*, Two-dimensional material-based electrochemical sensors/biosensors for food safety and biomolecular detection, *Biosensors*, 2022, **12**(5), 314.

6 D. Tyagi, *et al.*, Recent advances in two-dimensional-material-based sensing technology toward health and environmental monitoring applications, *Nanoscale*, 2020, **12**(6), 3535–3559.

7 L. Tang, *et al.*, NiCo layered double hydroxide nanosheet arrays constructed via in-situ plasma etching as non-enzymatic electrochemical sensor for glucose in food, *Microchem. J.*, 2024, **206**, 111496.

8 C. Li, M. Wei, D. G. Evans and X. Duan, Layered double hydroxide-based nanomaterials as highly efficient catalysts and adsorbents, *Small*, 2014, **10**(22), 4469–4486.

9 F. Wang, Y. Zhang, W. Liang, L. Chen, Y. Li and X. He, non-enzymatic glucose sensor with high sensitivity based on Cu-Al layered double hydroxides, *Sens. Actuators, B*, 2018, **273**, 41–47.

10 S. An, *et al.*, Co-Ni layered double hydroxides wrapped on leaf-shaped copper oxide hybrids for non-enzymatic detection of glucose, *J. Colloid Interface Sci.*, 2021, **592**, 205–214.

11 N. Hong, *et al.*, Co-precipitation synthesis of reduced graphene oxide/NiAl-layered double hydroxide hybrid and its application in flame retarding poly (methyl methacrylate), *Mater. Res. Bull.*, 2014, **49**, 657–664.

12 O. O. Balayeva, *et al.*, Synthesis of zinc-aluminum mixed oxide/polyvinyl alcohol (ZnAl mixed oxide/PVA) and application in Pb(II) removal from aqueous solution, *J. Dispersion Sci. Technol.*, 2021, **42**(10), 1482–1493.

13 W. Xu, B. Zhang, X. Wang, G. Wang and D. Ding, The flame retardancy and smoke suppression effect of a hybrid containing $CuMoO_4$ modified reduced graphene oxide/layered double hydroxide on epoxy resin, *J. Hazard. Mater.*, 2018, **343**, 364–375.

14 M. Li, J. Cheng, J. Wang, F. Liu and X. Zhang, The growth of nickel-manganese and cobalt-manganese layered double hydroxides on reduced graphene oxide for supercapacitor, *Electrochim. Acta*, 2016, **206**, 108–115.

15 N. Hosni, S. El-Sayed, A. M. El Sayed and S. Saber, Synthesis and modification of the structural, optical, and thermal properties of PVA–PEO by LDH nanoplates, *Phys. Scr.*, 2023, **98**(3), 035704.

16 J. Yaseen, F. Saira and Z. Batool, Synthesis of CuSe/PVP/GO and CuSe/MWCNTs for their Applications as Nonenzymatic Electrochemical Glucose Biosensor, *RSC Adv.*, 2024, 6895–6905.

17 B. Sriram, M. M. Stanley, S.-F. Wang, Y.-F. Hsu and M. George, Two-dimensional CuMn-layered double hydroxides: a study of interlayer anion variants on the electrochemical sensing of trichlorophenol, *Inorg. Chem.*, 2024, **63**(5), 2833–2843.

18 G. Zhao, *et al.*, Reduced graphene oxide modified NiFe-calcinated layered double hydroxides for enhanced photocatalytic removal of methylene blue, *Appl. Surf. Sci.*, 2018, **434**, 251–259.

19 O. O. Balayeva, *et al.*, Synthesis and characterization of CuxCd1-xS nanocrystals into functionalized nitrile butadiene rubber matrix, *J. Chin. Chem. Soc.*, 2024, **71**(6), 550–565.
20 G. B. B. Varadwaj, O. A. Oyetade, S. Rana, B. S. Martincigh, S. B. Jonnalagadda and V. O. Nyamori, Facile synthesis of three-dimensional Mg–Al layered double hydroxide/partially reduced graphene oxide nanocomposites for the effective removal of Pb^{2+} from aqueous solution, *ACS Appl. Mater. Interfaces*, 2017, **9**(20), 17290–17305.
21 H. Meskher, F. Achi, F. B. Moussa, A. Henni and H. Belkhelfa, A novel pentachlorophenol electrochemical sensor based on nickel-cobalt layered double hydroxide doped with reduced graphene oxide composite, *ECS Adv.*, 2023, **2**(1), 016503.
22 K. P. Sharma, M. Shin, G. P. Awasthi and C. Yu, Single step hydrothermal synthesis of CuS/MnS composite for electrochemical non-enzymatic glucose sensor, *Solid State Sci.*, 2023, **143**, 107279.
23 K. K. Sarigamala, S. Shukla, A. Struck and S. Saxena, Rationally engineered 3D-dendritic cell-like morphologies of LDH nanostructures using graphene-based core–shell structures, *Microsyst. Nanoeng.*, 2019, **5**(1), 65.
24 E. R. Cernei, A. Maxim, D. C. Maxim, R. B. Mavru and G. Zegan, Textural properties of amoxicillin-Anionic clays composites for possible oral diseases uses, *Rev. Chim.*, 2016, **67**, 1306–1308.
25 F. Liaqat, I. Ul Haq, F. Saira and S. Qaisar, Development of glucose sensor based on cobalt and nickel doped ceria nanostructures, *Mater. Sci. Eng.: B*, 2023, **289**, 116231.
26 G. Rathee, A. Awasthi, D. Sood, R. Tomar, V. Tomar and R. Chandra, A new biocompatible ternary Layered Double Hydroxide Adsorbent for ultrafast removal of anionic organic dyes, *Sci. Rep.*, 2019, **9**(1), 16225.
27 S. Naseem, S. P. Lonkar, A. Leuteritz and F. J. W. Labuschagné, Different transition metal combinations of LDH systems and their organic modifications as UV protecting materials for polypropylene (PP), *RSC Adv.*, 2018, **8**(52), 29789–29796.
28 F. L. Theiss, G. A. Ayoko and R. L. Frost, Thermogravimetric analysis of selected layered double hydroxides, *J. Therm. Anal. Calorim.*, 2013, **112**, 649–657.
29 F. Wang, Y. Zhang, W. Liang, L. Chen, Y. Li and X. He, Non-enzymatic glucose sensor with high sensitivity based on Cu-Al layered double hydroxides, *Sens. Actuators, B*, 2018, **273**, 41–47.
30 D. Tonelli, M. Tonelli, S. Gianvittorio and A. Lesch, LDH-Based Voltammetric Sensors, *Micromachines*, 2024, **15**(5), 640.
31 H. Li and P. Zhao, Amorphous Ni–Co–Fe hydroxide nanospheres for the highly sensitive and selective non-enzymatic glucose sensor applications, *J. Alloys Compd.*, 2019, **800**, 261–271.
32 S. Khataee, G. Dehghan, Z. Shaghaghi and A. Khataee, An enzyme-free sensor based on La-doped CoFe-layered double hydroxide decorated on reduced graphene oxide for sensitive electrochemical detection of urea, *Microchim. Acta*, 2024, **191**(3), 152.
33 C. Heyser, R. Schrebler and P. Grez, New route for the synthesis of nickel (II) oxide nanostructures and its application as non-enzymatic glucose sensor, *J. Electroanal. Chem.*, 2019, **832**, 189–195.
34 S. An, *et al.*, Co-Ni layered double hydroxides wrapped on leaf-shaped copper oxide hybrids for non-enzymatic detection of glucose, *J. Colloid Interface Sci.*, 2021, **592**, 205–214.
35 N. Shishegari, A. Sabahi, F. Manteghi, A. Ghaffarinejad and Z. Tehrani, Non-enzymatic sensor based on nitrogen-doped graphene modified with Pd nano-particles and NiAl layered double hydroxide for glucose determination in blood, *J. Electroanal. Chem.*, 2020, **871**, 114285.
36 O. González-Meza, E. Larios-Durán, A. Gutiérrez-Becerra, N. Casillas, J. Escalante and M. Bárcena-Soto, Development of a Randles-Ševčík-like equation to predict the peak current of cyclic voltammetry for solid metal hexacyanoferrates, *J. Solid State Electrochem.*, 2019, **23**(11), 3123–3133.
37 S. Mundinamani and M. Rabinal, Cyclic voltammetric studies on the role of electrode, electrode surface modification and electrolyte solution of an electrochemical cell, *J. Appl. Chem.*, 2014, **7**(9), 45–52.
38 D. Song, *et al.*, Three-dimensional hierarchical structure NiFe layered double hydroxides nanosheets based on carbon cloth for high performance non-enzymatic glucose detection, *Int. J. Electrochem. Sci.*, 2020, **15**(3), 1949–1963.
39 N. Rafique, *et al.*, Binder free 3D core–shell NiFe layered double hydroxide (LDH) nanosheets (NSs) supported on Cu foam as a highly efficient non-enzymatic glucose sensor, *J. Colloid Interface Sci.*, 2022, **615**, 865–875.
40 M. SG, P. S. Adarakatti, V. Udayakumar and A. S. Almalki, Fabrication of cerium oxide and β-Ni $(OH)_2$ nano hexagonal architectures assembled on reduced graphene oxide for non-enzymatic electrochemical detection of glucose, *Ionics*, 2022, **28**(4), 1957–1972.
41 Y. Nazish, S. Sabahat, R. S. Z. Saleem, F. Saira and A. Yaqub, Effect of nano-morphologies on catalysis and non-enzymatic glucose sensing, *J. Mater. Res.*, 2024, 804–820.
42 F. Saira, H. Razzaq, M. Mumtaz, S. Ahmad and M. A. Rafiq, Investigation of Glucose oxidation at Gold Nanoparticles deposited at Carbon Nanotubes modified Glassy Carbon Electrode by Theoretical and Experimental Methods, *Karbala Int. J. Mod. Sci.*, 2020, 124–131.
43 F. Saira, A. Yaqub and H. Razzaq, Hollow nanocages for electrochemical glucose sensing: A comprehensive review, *J. Mol. Struct.*, 2022, **1268**, 133646.
44 H. Tian, M. Jia, M. Zhang and J. Hu, Nonenzymatic glucose sensor based on nickel ion implanted-modified indium tin oxide electrode, *Electrochim. Acta*, 2013, **96**, 285–290.
45 W. Shen, J. Sun, J. Y. H. Seah, L. Shi, S. Tang and H. K. Lee, Needle-based sampling coupled with colorimetric reaction catalyzed by layered double hydroxide peroxidase mimic for rapid detection of the change of d-glucose levels with time in bananas, *Anal. Chim. Acta*, 2018, **1001**, 32–39.
46 S. Samuei, J. Fakkar, Z. Rezvani, A. Shomali and B. Habibi, Synthesis and characterization of graphene quantum dots/

CoNiAl-layered double-hydroxide nanocomposite: Application as a glucose sensor, *Anal. Biochem.*, 2017, **521**, 31–39.

47 Z. Yan, H. Zheng, J. Chen and Y. Ye, The micro network of polyacrylonitrile (PAN)-polyaniline (Pani)-graphene (GRA) hybrid nanocomposites for effective electrochemical detection of glucose and improved stability, *Int. J. Electrochem. Sci.*, 2019, **14**(3), 3011–3023.

48 S. Zhou, C. Hao, J. Wang, X. Wang and H. Gao, Metal-organic framework templated synthesis of porous NiCo2O4/ZnCo2O4/Co3O4 hollow polyhedral nanocages and their enhanced pseudocapacitive properties, *Chem. Eng. J.*, 2018, **351**, 74–84.

49 M. Mizuhata, Electrical conductivity measurement of electrolyte solution, *Electrochemistry*, 2022, **90**(10), 102011.

50 J. Jiang, L. Ai and L. Li, Synthesis and characterization of polyaniline-based nanocomposites containing magnetic Li–Ni–La ferrite, *J. Non-Cryst. Solids*, 2009, **355**(34–36), 1733–1736.

51 X. Hong, *et al.*, Recent progress on graphene/polyaniline composites for high-performance supercapacitors, *Materials*, 2019, **12**(9), 1451.

52 M. de Sá and C. M. Pereira, The relevance of the initial conditions in glassy carbon electrode sensing applications: the ferri/ferrocyanide redox reaction model system in aqueous solution, *Electrochim. Acta*, 2024, **489**, 144158.

53 S. Sabahat, M. Ejaz, F. Saira, R. S. Z. Saleem and Y. Nazish, Surface plasmon resonance-based synthesis of gold nanorods for sensing applications, *Chem. Pap.*, 2023, 5901–5911.